IEEE Access
Multidisciplinary | Rapid Review | Open Access Journal

Received August 18, 2021, accepted September 5, 2021, date of publication September 7, 2021,
date of current version September 16, 2021.

Digital Object Identifier 10.1109/ACCESS.2021.3111025

The Role of Space Charge on Corona Inception Threshold Conditions in Rod-Plane Air Gaps at DC/AC Combined Voltages

XUYUAN HE[1], YUNBO ZHOU[1], ZICHEN HE[1], JIE ZHU[2], LUXING ZHAO[3], (Senior Member, IEEE), BOYANG SHEN[4], (Member, IEEE), AND XINGMING BIAN[1], (Member, IEEE)

[1]State Key Laboratory of Alternate Electrical Power System with Renewable Energy Sources, North China Electric Power University, Beijing 102206, China
[2]State Grid Yangzhou Power Supply Company, Yangzhou, Jiangsu 225009, China
[3]China Electric Power Research Institute, Beijing 100192, China
[4]Electrical Engineering Division, University of Cambridge, Cambridge CB3 0FA, U.K.

Corresponding author: Xingming Bian (bianxingming@ncepu.edu.cn)

This work was supported in part by the National Natural Science Foundation of China under Grant 51877082, in part by the State Key Laboratory of Reliability and Intelligence of Electrical Equipment under Grant EERIKF2019002, and in part by the Fundamental Research Funds for the Central Universities under Grant 2019MS011.

ABSTRACT This work investigates the corona inception voltage and the motion of space charge near a rod-plane electrode under combined DC-AC voltages. For a high AC component, the corona inception voltage of the equivalent negative corona exceeds that of the equivalent positive corona. For a small AC component, the corona inception voltage of the equivalent positive corona exceeds that of the equivalent negative corona. The corona inception voltage decreases with increasing AC component. The charge-motion model based on hydrodynamics is used to analyze the charge motion for different AC/DC voltage ratios. The charge remaining for equivalent negative coronas exceeds that for equivalent positive coronas with high AC components. In addition, the charge remaining for equivalent positive coronas exceeds that of equivalent negative coronas with small AC components. As the AC component decreases, the remaining space charge increases. The results show that space charge tends to ''block'' corona inception. The more space charge remains, the higher the corona inception voltage is. Therefore, the variation in space charge and the corona inception threshold conditions under combined DC-AC voltage differ from those under only DC or AC voltage.

INDEX TERMS Corona discharge, corona inception, DC/AC combined voltages, space charge.

I. INTRODUCTION

Nowadays, with the expansion of the transmission grid in China, the lack of space for new power transmission lines is becoming a serious problem. To conserve land resources and improve transmission capacity, the DC-AC hybrid transmission line has been widely studied [1]–[3]. When the electric field on the electrode is above the corona inception, corona discharge will occur. Corona discharge can release a large of space charge [4] and lead to energy loss, audible noise, radio interference and insulation degradation [5]–[9].

The associate editor coordinating the review of this manuscript and approving it for publication was Mohd Zainal Abidin Ab Kadir.

Compared with a DC or AC transmission line, the electromagnetic environment of a DC-AC hybrid transmission is more complex [3], which makes it more challenging to ensure the safety of transmission lines and electrical components.

The corona inception voltage is a key factor in the design of transmission lines and electrical components and electromagnetic environment optimization [10]–[12]. Corona inception field is an important criterion when predicting the acoustic noise and radio interference of transmission lines [13]. In the study of corona under AC-DC combined voltage, scholars mostly use the reduced-scale transmission line model [14]. In the calculation of transmission line models, most of them use the peek's formula to calculate corona inception field

of the wire [15]. For the electric field on the wire surface, in order to reflect the effect of voltage variation and space charge, some scholars discard the Deutsch hypothesis and use the improved numerical algorithm in the model to calculate the electric field on the wire surface [4], [16]. However, for the complex electrode structures under the influence of AC-DC combined voltage, such as commutation valves. For the corona occurring at complex electrode structures, the corona inception criteria is usually used to obtain the corona inception voltage and corona inception field [17]–[20]. The corona inception voltage can be affected by space charge and other environmental factors [21]–[24].

Corona discharge generates a large amount of space charge, which enhances the synthetic field near the ground beneath the transmission line [1]. The space charge released by a corona discharge weakens the electric field near the electrode [22], [25], which renders corona inception more difficulties. Accumulated positive ions in the positive corona inhibit the formation of further streamers [26]. In addition, space charge influences the generation of Trichel pulse. The falling edge of the Trichel pulse is dominated by negative ions [27], [28], which reduces the electric field and cuts off the electron avalanche in the negative corona [29]. In the case of superposition of AC voltage and DC voltage, it is inevitable to consider the reciprocal motion of space charge under the AC voltage. Previous studies show that in the transmission line model, the AC voltage has negligible effect on the charge generated by the DC conductor [2]. However, it is questionable whether this conclusion also applies to short-gap model such as rod-plane model.

The study of space charge under combined DC-AC voltage mainly focuses on the low-frequency corona current due to the motion of the ion cloud [3], [30], [31], partial discharge in oil-paper insulation [32], [33], combined field strength near the ground [14], and the ion flow field [34], [35]. The ion flow field model neglects the ionosphere layer [36], [37]. However, in corona inception models, the ionosphere layer is not generally ignored [38]–[40]. Therefore, hydrodynamic models are commonly used to study the space charge and electric field at corona inception [41], [42]. For short gap electrodes, Qi and Zhou studied the partial discharge (PD) and found the inception voltage of PD increases as the DC component increasing because of the reverse electric field generated by charge [32], [43]. However, there are few micromechanical explanations for the corona inception characteristics under DC-AC combined voltage at the rod-plane electrode. Some phenomena different from pure DC and AC corona have not been studied yet. Therefore, it is worthwhile to consider simultaneously the space charge and the corona inception voltage and determine how they are related.

This study discusses the threshold conditions for corona inception under combined DC-AC voltage. Defining a uniform corona inception voltage allows synchronous current and voltage measurements to be made and thereby to obtain the corona inception voltage for different ratios of AC to DC components. Based on experiments, we develop a fluid model of space charge motion. Considering the effects of space charge, the corona inception voltage is analyzed under different conditions and compared from the perspective of space charge.

II. EXPERIMENTAL SETUP

An experiment on the corona inception voltage of rod-plane electrode at combined DC-AC voltage was carried out.

A. EXPERIMENTAL PLATFORM

Fig. 1 shows the experimental platform. The ambient temperature for experiments was around 14 ± 1 °C, and the relative humidity was 25% ± 2%. The rod-plane electrode was composed of a hemispherical copper rod and a disk. The rod radius was 1.5 mm, the disk radius was 20 cm, and the bottom end of the rod was 1-4 cm from the disk. The plane was connected to a DC voltage power through a 1.34 MΩ protection resistor, and the rod was connected to the AC power through a 10.27 MΩ protection resistor. DC power and AC power were added to the two ends of rod and plane. Physical isolation of DC and AC power was supplied to avoid interference between them. Circuit connection diagram of the experimental platform is shown in Fig. 2 and some physical views of experimental equipment are shown in Fig. 3.

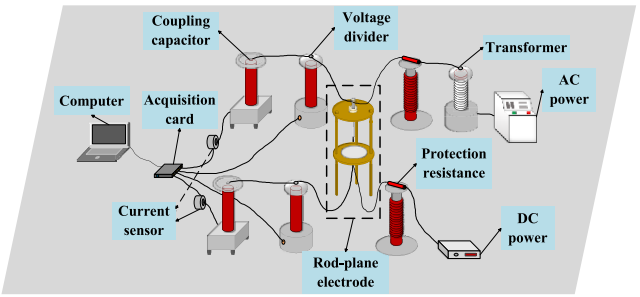

FIGURE 1. Experimental platform for corona of rod-plane electrode at DC-AC combined voltage.

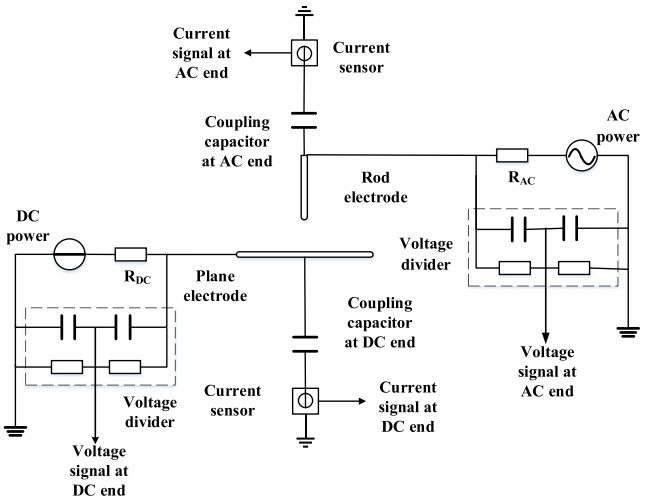

FIGURE 2. Circuit connection diagram of the experimental platform.

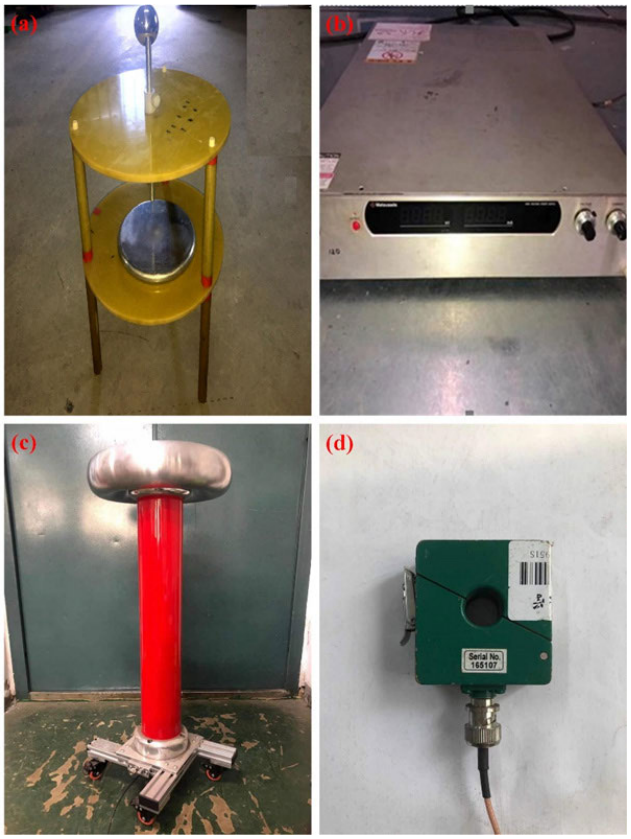

FIGURE 3. (a) The rod-plane electrode. (b) The power supply. (c) The coupling capacitor. (d) The current sensor.

When a corona occurs, the signal of the corona current in the plane was transmitted to the acquisition card through a coupling capacitor of 100 pF, and the DC voltage signal from the plane was transmitted to the acquisition card through a voltage divider with ratio of 1:1000. The corona current signal and AC voltage signal at the rod were then transmitted to the acquisition card through a 1050 pF coupling capacitor and a 1:1000 voltage divider. The current and voltage signals were simultaneously acquired by the PC via a four-channel acquisition card at a sampling frequency of 5 GS/s. And the current signal was detected by Person probes which can measure currents from 1.5 kHz to 200 MHz. The detailed experimental equipment parameters are shown in Table 1. To reduce the effect of noise on the measurement, the band-pass filtering method was used to process the current single data and the lowpass filtering method was used to process the DC/AC voltage single. The range of bandpass filtering was from 10 kHz to 200 MHz, which can pass most of the corona current pulse component and filter out a significant portion of the noise component [44]. And the maximum frequency of lowpass filtering is 1kHz, which can filter out the most noise components.

B. MEASUREMENTS OF CORONA INCEPTION VOLTAGE

Fig. 4 shows the DC voltage, AC voltage and the corona current pulse signal when the AC voltage was fixed at 2 kV.

TABLE 1. Parameters of experimental equipment.

Equipment	Parameters
Positive DC Voltage Source	Model: Matsusada AU-80, Maximum Output: 80 kV, Accuracy: 0.1 kV, Ripple Coefficient: 0.1%. Maximum Output Current: 10 mA
Negative DC Voltage Source	Model: Matsusada AU-120, Maximum Output: 120 kV, Accuracy: 0.1 kV, Ripple Coefficient: 0.1%. Maximum Output Current: 10 mA
AC voltage Source	Model: GDYT-15 kVA, Maximum Effective Value Output: 150 kV, Maximum Output Current: 100 mA
DC Protection Resistance	R=1.34 MΩ
AC Protection Resistance	R=10.27 MΩ
Four-channel acquisition card	Model: PicoScope 6000, Maximum single channel sampling rate: 5GS/s, Bandwidth: 500MHz, Sampling buffer storage: 2G.
Coupling capacitor at DC end	C_{DC}=100pF
Coupling capacitor at AC end	C_{AC}=1050pF
Current sensor	Model: Person 8585C， Frequency response range: 1.5kHz~200MHz.
Voltage Divider	Model: GDFR-150, Rated Voltage Ratio: 1000:1, DC Accuracy: 0.5%, AC Accuracy: 1%

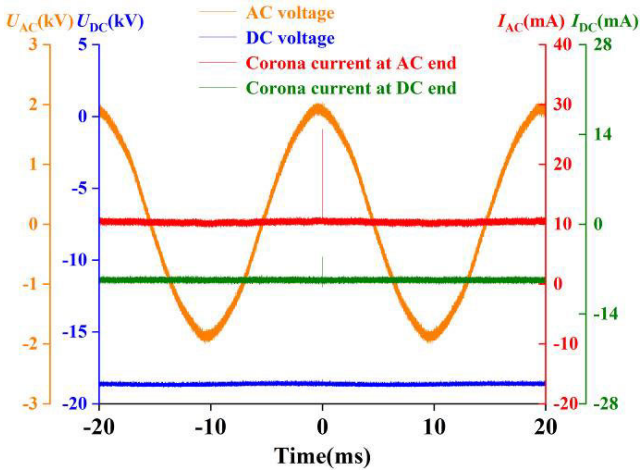

FIGURE 4. Measured current and voltage signal at rod and plane.

The DC voltage was 18.60kV. The corona current pulse was occurring near the peak of AC voltage. Because corona discharge is a probabilistic event, the corona pulse was recorded 30 times for each voltage case, and the AC voltage

corresponding to expected value of the normal distribution of corona pulses was taken as the actual AC component at the time of corona inception. The AC voltage was fixed at a certain value, and the DC voltage was gradually increased in increments of 0.1 kV. The voltage was held constant for 10 s after each voltage increment. The fixed value of AC voltage was 0 kV at the beginning, and the AC voltage was increased by 2 kV each time until the moment before AC corona occurring. When the corona pulse in Fig. 5 appears, the corona occurs. The corona current pulse is appearing in the both rod and plane at the same moment. The current probe can capture two types of pulses at the same time. The corresponding DC and AC components were recorded at this time. The advantage of using the corona current pulse method to detect the corona moment is that it is sensitive and accurate, and the phase information corresponding to the corona current can be detected. The experiments were done for rod-plane distances $D = 1, 2, 3$ and 4 cm.

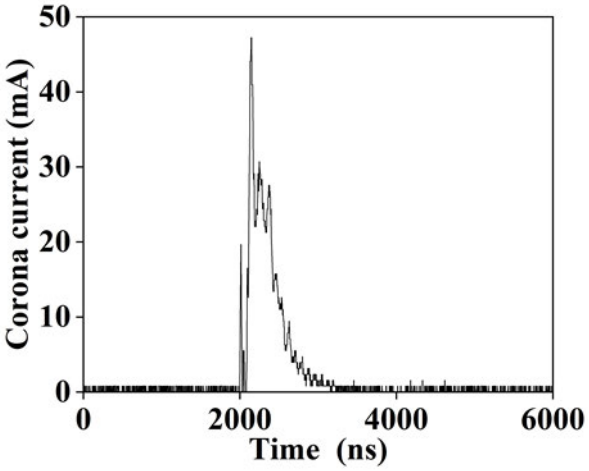

FIGURE 5. Measured corona pulse signal.

The DC voltage at the time of corona inception is taken as the DC component, denoted U_{DC}, and the instantaneous value of AC voltage at the corona pulse occurring is taken as the AC component, denoted U_{AC} or $U\sin(\omega t + \theta)$, which the U is the magnitude of AC voltage, ω is the Angular frequency of AC voltage, t is the time of corona pulse appearing and the θ is the initial phase of AC voltage. It should be noted that due to the uncertainty in the appearance of corona pulses, each θ is selected after 30 pulses captured, and the median of the normal distribution of the pulses is selected. The ratio U_{AC}/U_{DC} at the corona inception varies because AC voltage differs each time. For comparison, the corona that occurs when U_{r-p} (i.e., the rod-plane potential difference) is positive is considered the equivalent positive corona (EPC) [Fig. 6(a) and Fig. 6(c)]. The corona that occurs when the U_{r-p} is negative is considered the equivalent negative corona (ENC) [Fig. 6(b) and Fig. 6(d)].

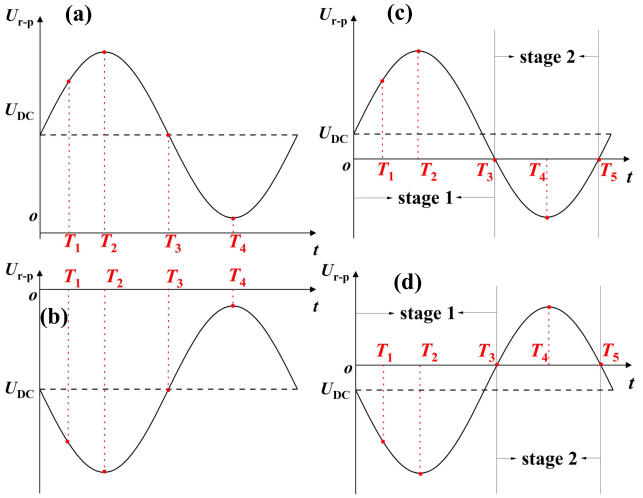

FIGURE 6. (a) U_{r-p} for equivalent positive corona with high U_{DC}. (b) U_{r-p} for equivalent negative corona with high U_{DC}. (c) U_{r-p} for equivalent positive corona with high U_{AC}. (d) U_{r-p} for equivalent negative corona with high U_{AC}.

C. EXPERIMENTAL RESULTS

Fig. 7(a) and Fig. 7(b) show that U_{DC} decreases as U_{AC} increases for both EPC and ENC. When U_{AC} is small, the potential U_{DC} required for EPC is higher than that required for ENC with the same U_{AC}. Conversely, when U_{AC} is high, the potential U_{DC} required for EPC is lower than that required for ENC. For $D = 2$ cm, the curves of EPC and ENC intersect at point P_2, while in the case of $D = 4$ cm, they intersect at point P_4. For comparison, the U_{AC} and U_{DC} are called high U_{AC} and U_{DC} when they are higher than the value of intersection point, while the opposite is called low U_{AC} and U_{DC}.

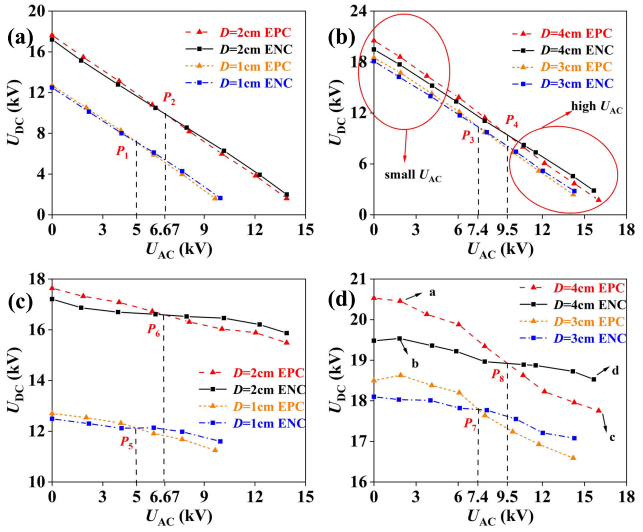

FIGURE 7. (a)-(b) Measured U_{DC} and U_{AC} when corona occurs at D = 1-4cm. (c-d) Relationship between U_{AC} and U_i at D = 1-4cm.

No accepted definition exists for corona-inception voltage for a combined DC-AC voltage. We therefore propose, given

the small gap between the rod and plane, to define the combined DC-AC corona inception voltage U_i between the rod and plane as:

$$U_i = U_{AC} + U_{DC} = U\sin(\omega t + \theta) + U_{DC} \tag{1}$$

Fig. 8 gives the relationship among U_{AC}, U_{DC}, and U. The initial phase of AC voltage θ is set as 0°.

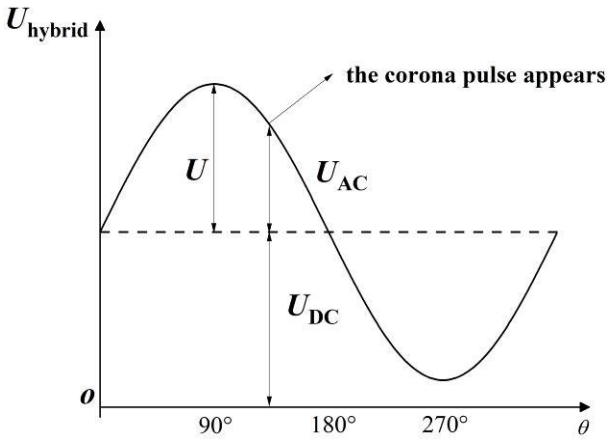

FIGURE 8. The voltage waveform of superimposed DC and AC voltages.

For $D = 4$ cm, Fig. 7(d) shows that, as U_{AC} increases, U_i decreases for both EPC and ENC. When U_{AC} is small, the equivalent negative corona-inception voltage, denoted U_i^n, is smaller than the equivalent positive corona inception voltage, denoted U_i^p. U_i^n is 4.51% less than U_i^p when AC voltage is 2 kV as points a and b shown in Fig.7(d). When U_{AC} is high, $U_i^p < U_i^n \cdot U_i^p$ is 4.16% less than U_i^n when the $U \approx 16$ kV as points c and d shown in Fig.7(d). This is different from ether DC corona or AC corona. When $U_{AC} \approx 9.50$ kV, the curves of EPC and ENC intersect at point P_8. When $D = 2$ cm, the relationship between the U_i and the U_{AC} is similar to that when $D = 4$ cm, but U_i is smaller and the intersection of EPC and EAC is at point P_6.

The variation in potential difference between the rod-plane gap under a combined DC-AC voltage with varying AC/DC ratios can be divided into the following four cases: Fig. 6(a) shows the EPC when U_{DC} is high, Fig. 6(b) shows the ENC when U_{DC} is high, Fig. 6(c) shows the EPC when U_{AC} is high, and Fig. 6(d) shows the ENC when U_{AC} is high. Each of these four cases corresponds to the four cases a–d in Fig. 7(d). The potential difference between rod and plane is not reversed in cases a and b. In cases c and d, the potential difference is reversed in polarity, which, over a cycle, first goes through the positive (negative) phase and then through the negative (positive) phase. The first phase is defined as stage 1 and the second phase is defined as stage 2, as shown in Fig. 6(c) and Fig. 6(d). The corona occurs in stage 1. The typical moments T_1 - T_4 in Fig. 6(a) and Fig. 6(b) and T_1 - T_5 in Fig. 6(c) and Fig. 6(d) are selected for analysis. The movement of charge differs in the four cases, which leads to different values of U_i in the four cases.

III. NUMERICAL STUDIES

A. CORONA FLUID MODEL

To find the connection between space charge and U_i, we developed a model to compute the space charge density and distribution at combined DC-AC voltage. The model is based on the continuity equations and Poisson's equation:

$$\begin{cases} \dfrac{\partial N_e}{\partial t} + \nabla\cdot(-D_e\nabla N_e + \boldsymbol{W_e}N_e) = R_e \\ R_e = \alpha N_e|\boldsymbol{W_e}| - \eta N_e|\boldsymbol{W_e}| - \beta_{ep}N_eN_p + S_t \end{cases} \tag{2}$$

$$\begin{cases} \dfrac{\partial N_p}{\partial t} + \nabla\cdot(-D_p\nabla N_p + \boldsymbol{W_p}N_p) = R_p \\ R_p = \alpha N_e|\boldsymbol{W_e}| - \beta_{ep}N_eN_p - \beta_{np}N_nN_p + S_t \end{cases} \tag{3}$$

$$\begin{cases} \dfrac{\partial N_n}{\partial t} + \nabla\cdot(-D_n\nabla N_n + \boldsymbol{W_n}N_n) = R_n \\ R_n = \eta N_e|\boldsymbol{W_e}| - \beta_{np}N_nN_p \end{cases} \tag{4}$$

$$\nabla^2\varphi = -\frac{e(N_p - N_e - N_n)}{\varepsilon_0} \tag{5}$$

$$\boldsymbol{E} = -\nabla\varphi \tag{6}$$

where φ indicates the electric potential; $\boldsymbol{E}$ is the electric field; N_e, N_p, and N_n are the electron, positive ion, and negative ion densities, respectively; e is the elementary charge; S_t is the photoionization term; ε_0 is the dielectric constant of air; α is the collision-ionization coefficient; η is the adsorption coefficient; $\boldsymbol{W_e}$, $\boldsymbol{W_p}$, and $\boldsymbol{W_n}$ are the velocity vectors for electrons and positive and negative ions, respectively; β_{ep} is the electron–positive-ion complex rate; β_{np} is the positive-ion–negative-ion composite rate; and D_e, D_p, and D_n are the diffusion coefficients for electrons, positive ions, and negative ions, respectively.

Fig. 9 shows the calculation domain and boundary of the model. U_{r-p} can be reversed at combined DC-AC voltage. Therefore, the EPC and ENC are modelled separately,

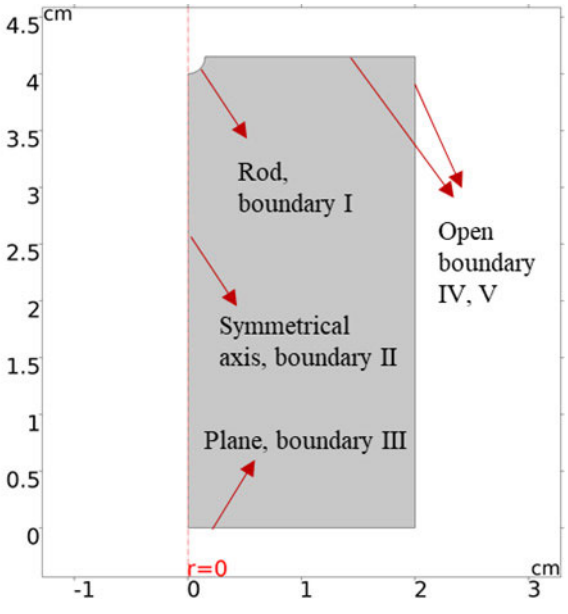

FIGURE 9. Numerical model calculation domain.

with positive corona boundary condition for positive U_{r-p} and negative corona boundary condition for negative U_{r-p}. The boundary conditions of continuity equation are shown in Table. 2 and Table. 3, where $\boldsymbol{n}$ is unit normal vector.

TABLE 2. Positive boundary condition.

Type of charge	Boundary I	Boundary III	Boundary IV, V
electron	$\boldsymbol{n}\cdot(-D_e\nabla N_e)=0$	$N_e=0$	$-\boldsymbol{n}\cdot(-D_e\nabla N_e)=0$
Positive ion	$N_p=0$	$\boldsymbol{n}\cdot(-D_p\nabla N_p)=0$	$-\boldsymbol{n}\cdot(-D_p\nabla N_p)=0$
Negative ion	$\boldsymbol{n}\cdot(-D_n\nabla N_n)=0$	$N_n=0$	$-\boldsymbol{n}\cdot(-D_n\nabla N_n)=0$

TABLE 3. Negative boundary condition.

Type of charge	Boundary I	Boundary III	Boundary IV、V
electron	$-\boldsymbol{n}\cdot(D_e\nabla N_e-N_e\boldsymbol{W}_e)=\gamma N_p\lvert\boldsymbol{W}_p\rvert$	$\boldsymbol{n}\cdot(-D_e\nabla N_e)=0$	$-\boldsymbol{n}\cdot(-D_e\nabla N_e)=0$
Positive ion	$\boldsymbol{n}\cdot(-D_p\nabla N_p)=0$	$N_p=0$	$-\boldsymbol{n}\cdot(-D_p\nabla N_p)=0$
Negative ion	$N_n=0$	$\boldsymbol{n}\cdot(-D_n\nabla N_n)=0$	$-\boldsymbol{n}\cdot(-D_n\nabla N_n)=0$

The parameters of the model are shown in appendix [45].

B. CORONA INCEPTION CRITERION

U_{AC} and U_{DC} at corona inception are computed by using the corona inception criterion based on photon effect [17], which demands that the number of photons produced by the secondary electron collapse is greater than the number of photons produced by the primary electron collapse.

As shown in Fig. 10, the bottom of the rod is the origin, and the central axis is the z axis. The corona inception criterion is computed on the z axis. For the EPC, when an electron arrives at the surface of the rod electrode from position z on the central axis, it produces multiple impact ionization. The total number of electrons produced by this electron is:

$$N_e(z)=\exp(-\int_z^0[\alpha(z')-\eta(z')]dz') \tag{7}$$

where z' is the virtual integral variable.

Considering the adsorption process of electrons in air, the total number of positive ions produced by the electron is not equal to (7), it should be:

$$N_p(z)=\int_0^z\alpha(z')\cdot(\exp(-\int_{z'}^z[\alpha(z'')-\eta(z'')]dz''))dz' \tag{8}$$

where z'' is also the virtual integral variable. The (8) can also represent the number of impact ionizations.

Supposing that the electron is triggered at the ionization boundary z_i, it produces a large number of excited particles by impact ionization as it moves towards the rod. When these excited-state particles jump back to the ground state, a lot of photons are released. If the probability of an impact

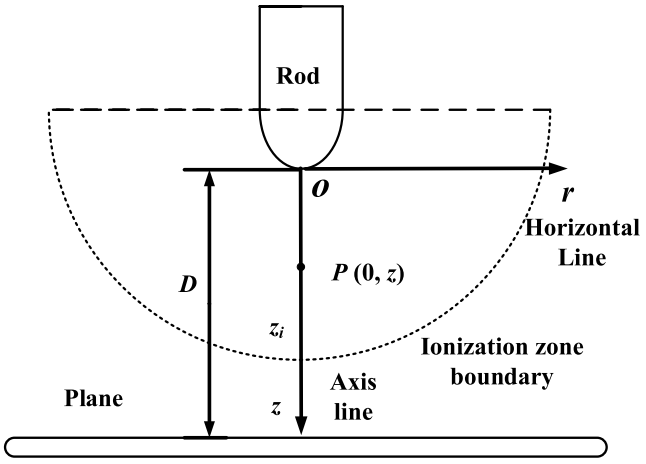

FIGURE 10. Diagram of computation of corona inception criterion.

collision producing a photon is proportional to the number of collisions, the number of photons produced by the primary electron avalanche is:

$$N_1=f_1N_p(z_i) \tag{9}$$

where f_1 is the probability of producing a photon per collision; z_i is the ionization boundary.

The following is the analysis of secondary electron avalanche. The gas molecules in space absorb the photons and produce photoelectrons. The photoelectrons continue moving towards the rod and repeat the process of primary electron avalanche. When the N_1 photons produced by the primary electron avalanche are emitted from the surface of the electrode, the total number of photons produced by all secondary electron avalanches is:

$$N_2(z)=f_1f_2N_1\int_0^{z_i}\mu N_p(z)\exp(-\mu(z))g_p(z)dz \tag{10}$$

where μ is the photon-absorption coefficient of air; and $g_p(z)$ is the area factor of the rod-plane electrode when a positive voltage is applied [46]; f_2 is the probability that a gas molecule absorbs a photon to produce a photoelectron.

To form a corona discharge, the number of photons generated by the secondary electron avalanche is larger than the number of primary electron avalanche photons:

$$N_2\geq N_1 \tag{11}$$

Considering the collision process of electrons very close to the electrode and the collision ionization coefficient is much larger than the attachment coefficient, the total number of positive ions in an electron avalanche can be simplified as:

$$N_p(z)\approx\exp(\int_0^z[\alpha(z')-\eta(z')]dz')-1 \tag{12}$$

Organizing the above equations, the corona inception criterion for EPC can be obtained as:

$$f_1f_2\int_0^{z_i}\mu(\exp(-\int_z^0[\alpha(z')-\eta(z')]dz')-1)\cdot\exp(-\mu z)g_p(z)dz\geq 1 \tag{13}$$

In the case of ENC, the photons absorbed by air molecules to generate photoelectrons are no longer considered, but the process of positive ions bombarding the cathode to produce electrons is considered. The corona inception criterion for ENC can be obtained as:

$$f_1 f_2 \int_0^{z_i} \alpha(z) \exp\{\int_0^z [\alpha(z') - \eta(z')]dz'\} \exp(-\mu z) g_n(z) dz \geq 1 \quad (14)$$

where the $g_n(z)$ is the area factor when the negative voltage is applied to the rod-plane electrode. At the end of stage 2, the corona inception moment of the next cycle is computed for EPC and ENC.

C. THE CASE OF HIGH U_{AC}

When U_{AC} is high in Fig. 6(c) and Fig. 7(d), five moments $T_1 - T_5$ are chosen when $U \approx 16.0$ kV and $D = 4$cm. T_1 is the moment when the AC voltage is half the amplitude. T_2 is the point at the maximum AC voltage in stage 1, T_3 is the point at the end of stage 1, T_4 is the highest point of stage 2, and T_5 is the point at the end of stage 2. In the experiment, when U is fixed about 16.0 kV, the U_i^p (16.12sin96.69° + 1.75) kV = 17.76 kV and the U_i^n = (15.8sin 82.61° + 2.86) kV = 18.83 kV. The following simulation calculations are performed for these two cases of corona inception. Table. 4 and Table. 5 list the moments and the corresponding AC voltages (magnitudes) for the EPC and the ENC. The model first calculates the charge distribution in one cycle. Then the charge distribution of the first cycle is used as the initial value to calculate the corona inception voltage for the next cycle.

TABLE 4. Location of the T_1-T_4 and corresponding AC voltage in EPC.

EPC	T_1	T_2	T_3	T_4	T_5
Stage	1	1	1	2	2
Time (ms)	1.67	5.00	10.35	15.00	19.65
AC voltage (kV)	8	16.00	-1.76	-16.00	1.76

TABLE 5. Location of the T_1-T_4 and corresponding AC voltage in ENC.

ENC	T_1	T_2	T_3	T_4	T_5
Stage	1	1	1	2	2
Time (ms)	1.67	5.00	10.57	15.00	19.43
AC voltage (kV)	-8	-16.00	2.83	16.00	-2.83

Fig. 11(a) and Fig. 11(b) show the space charge distribution of EPC and ENC before the corona inception at T_1. Both the EPC and ENC have a small amount of space charge. The number of space charges keeps increasing slowly with time. The space charges in both are dominated by positive ions. The ions increase the field strength near the rod of ENC on the one hand, and decrease the field strength near the rod of EPC on the other hand.

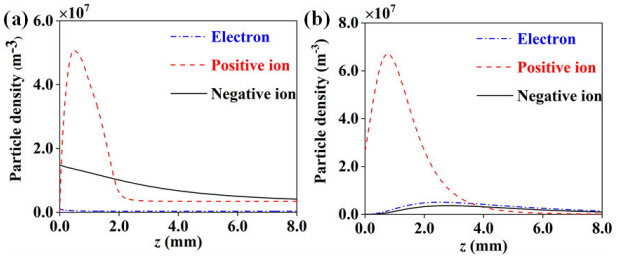

FIGURE 11. (a) Computed charge density on the axis for the EPC at T_1, (b) Computed charge density on the axis for the ENC at T_1.

For the EPC, Fig. 12(a) and Fig. 12(b) show the charge of the electrons and of the positive and negative ions on the axis in stage 1. The space charge is dominated by positive ions and increases rapidly at T_2, which move away from the rod head due to the action of the electric field. A similar charge distribution can be found in [26], where the maximum density of positive ions on the axis is 2.12×10^{19} m^{-3}. When stage 1 ends (at T_3), the residual density of positive ions on the axis is 8.73×10^{16} m^{-3}. Since the densities of the three particles are not in the same order of magnitude, the diagrams of the densities of non-dominant particles at T_3, T_4 and T_5 in space are shown in Fig. 14 and Fig. 15.

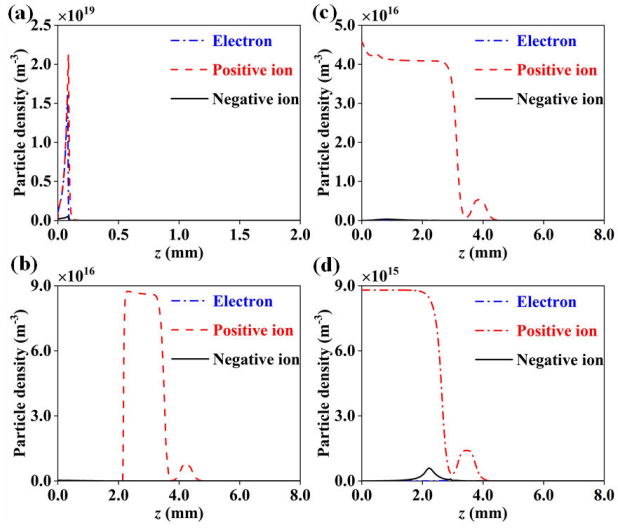

FIGURE 12. (a)–(d) Computed charge density on the axis for the EPC at T_2, T_3, T_4 and T_5.

Fig. 12(c) shows the variation in charge on the axis of the EPC after entering stage 2. The electric field is reversed at T_4. The positive charge of the EPC moves toward the rod and gradually decreases. In addition, the positive ions enter the rod electrode, triggering the cathode to emit photoelectrons, further depleting the positive ions.

Fig. 12(d) shows the positive ion density for the EPC at T_5. The maximum density of positive ion residues at T_5 is 8.8×10^{15} m^{-3}. These positive ions suppress the corona discharge in the next cycle.

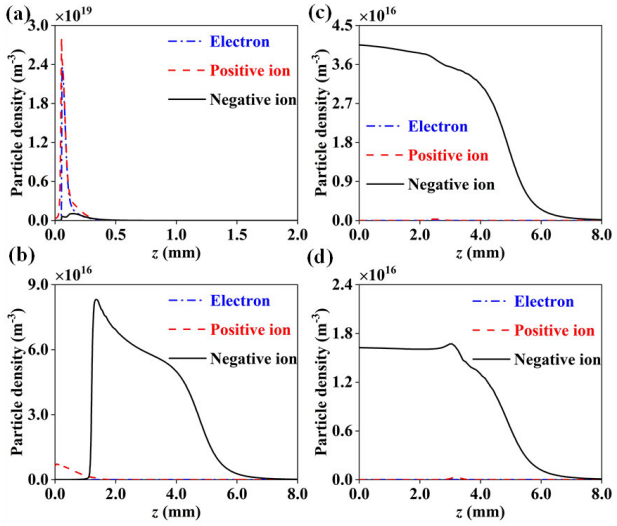

FIGURE 13. (a)–(d) Computed charge density on the axis for the ENC at T_2, T_3, T_4 and T_5.

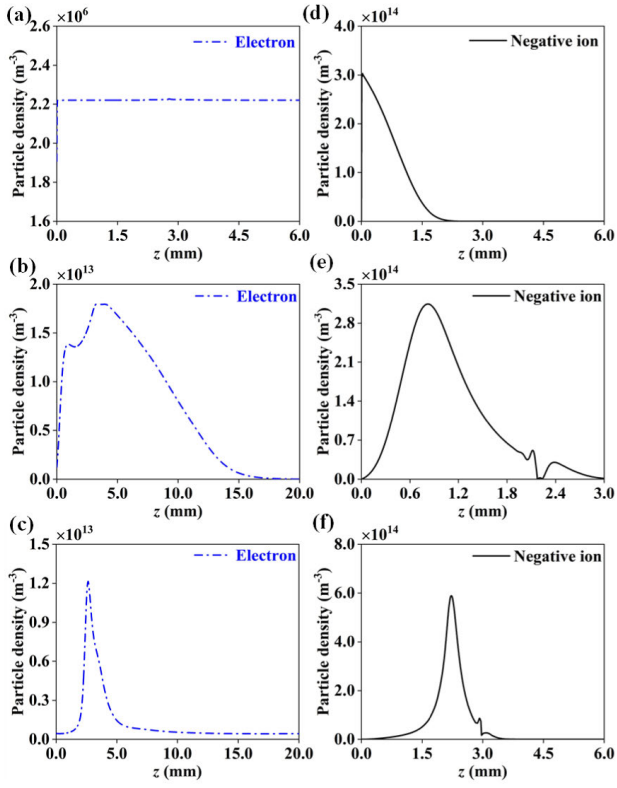

FIGURE 14. (a)-(c) Computed electron density on the axis for the EPC at T_3, T_4, and T_5. (d)-(f) Computed negative ions density on the axis for the EPC at T_3, T_4, and T_5.

Fig. 13(a) and Fig. 13(b) show the variation of electrons and positive and negative ions on the axis in stage 1 for the ENC. The space charge increases rapidly at T_2, which is the inception of the ENC for stage 1. Positive ions and electrons dominate the negative corona at T_2. From the end of the corona until T_3, positive ions gradually enter the head

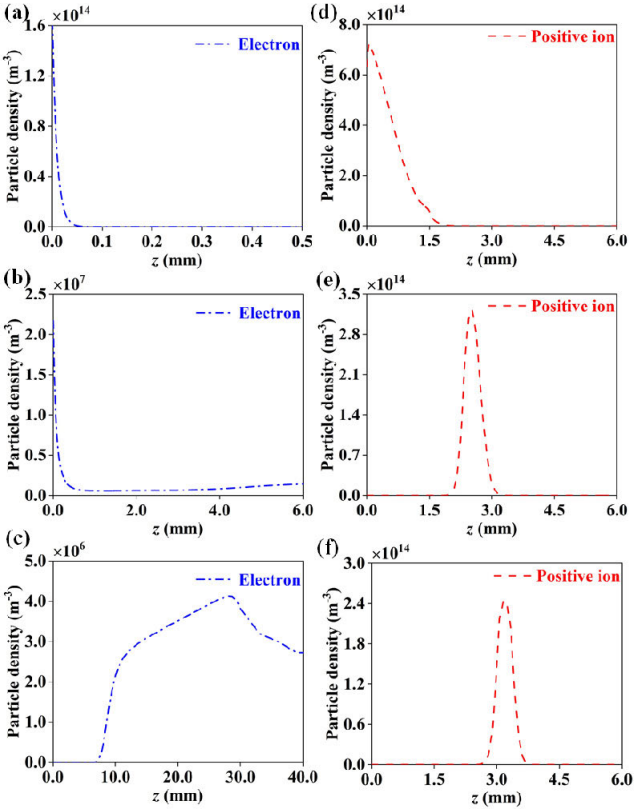

FIGURE 15. (a)-(c) Computed electron density on the axis for the ENC at T_3, T_4, and T_5. (d)-(f) Computed positive ions density on the axis for the ENC at T_3, T_4, and T_5.

of the rod and disappear. Negative ions accumulate on the outside of the rod and move away from the rod, so the space charge gradually becomes dominated by negative ions. At T_3, the maximum density of negative ions is 8.31×10^{16} m^{-3}.

Fig. 13(c) shows the variation of charge on the axis for the ENC after entering stage 2. At point T_4, the electric field is reversed, and the negative charge dominates the space charge. The negative charge moves toward the rod head and gradually decreases.

Fig. 13(d) shows when stage 2 ends (at T_5), the maximum density of residual negative ions for the ENC is 1.67×10^{16} m^{-3}. These negative ions act as a barrier in the next cycle of corona.

Fig. 14 shows the variation of electrons and negative ions at T_3, T_4, and T_5 for the EPC. Fig. 15 shows the variation of electrons and positive ions at T_3, T_4, and T_5 for the ENC. For electron and negative ion in EPC and electron and positive ion in ENC, their orders of magnitudes are smaller compared to the dominant charge (positive ion for EPC and negative for ENC). Due to the presence of cathode secondary emission in stage 2 for EPC, the density of electrons increases after the moment T_3. For the same reason, the negative ion grows in density from T_3 to T_5 as it moves away from the rod head. In the case of ENC, the density of electron is close to 0 at T_4 and T_5 because there is no cathode secondary emission in stage 2 of the ENC. The positive ions in the ENC are moving away from the rod and decreasing from T_3 to T_5.

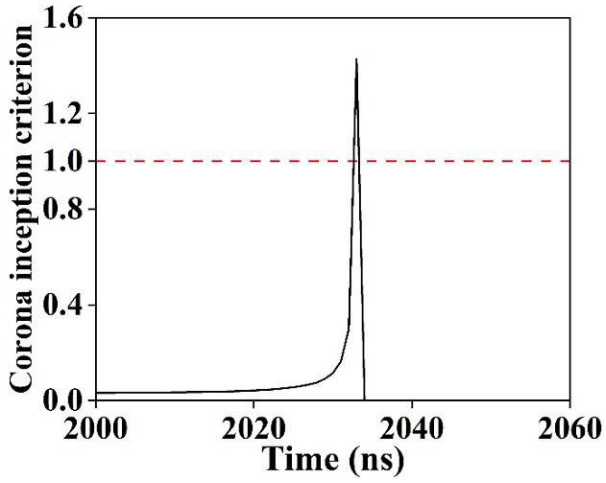

FIGURE 16. Computation of corona inception criterion.

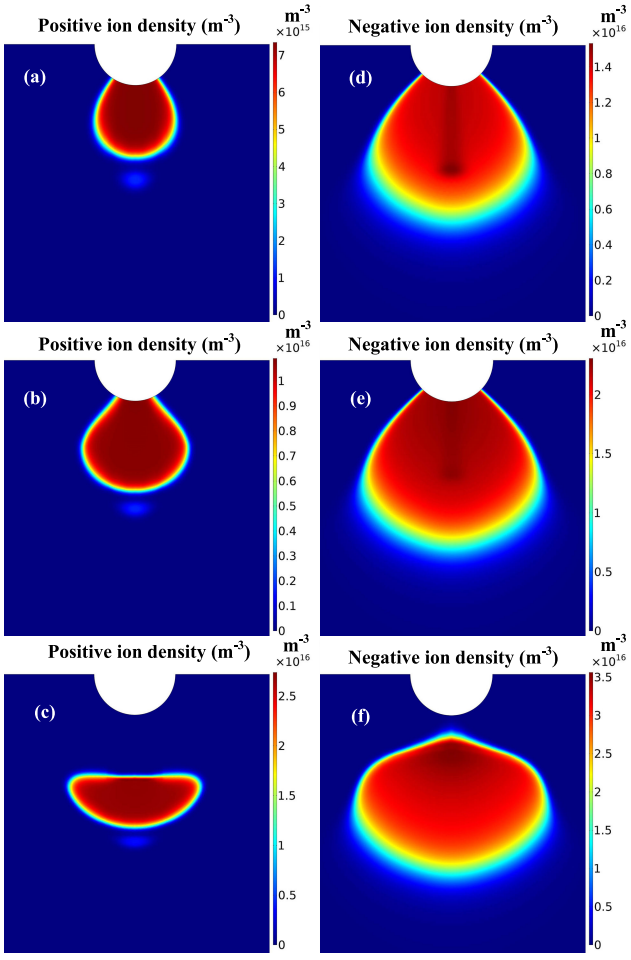

FIGURE 17. (a)–(c) Computed charge density at T_5 for EPC when U_{AC} = 16, 14, and 12 kV. (d)–(f) Computed charge density at T_5 for ENC when U_{AC} = 16, 14, and 12 kV.

At T_5, less positive ion of the EPC remains than negative ion of the ENC because secondary electron emission from positive ions bombards the cathode in stage 2 of the EPC. The presence of these electrons consumes an additional portion of the positive ions. In contrast, no such process exists for the ENC in stage 2. Therefore, the space charge produces more of an obstacle for the ENC in the next cycle.

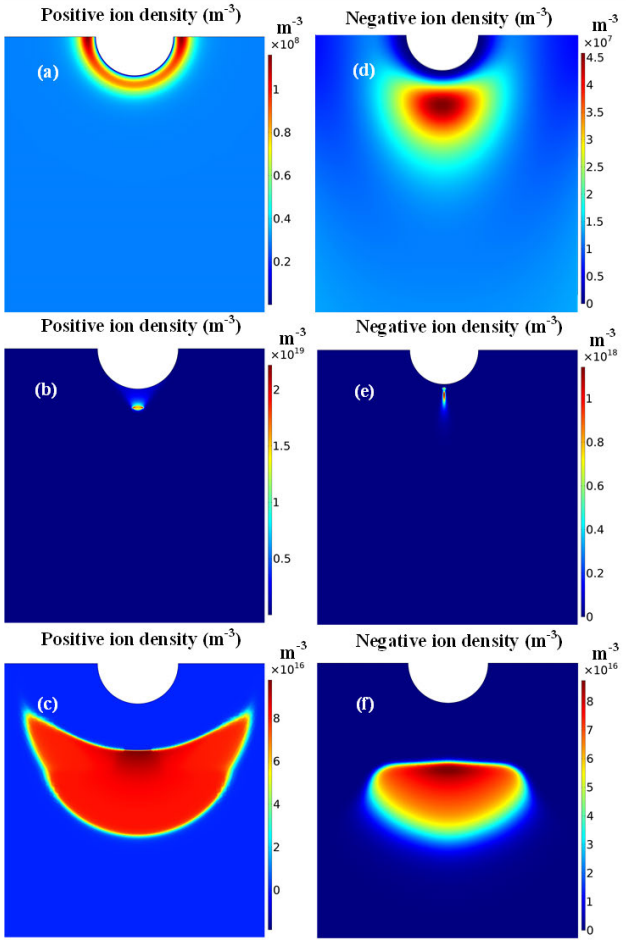

FIGURE 18. (a)-(c) Computed charge density at T_1-T_3 for EPC for U_{AC} = 8 kV. (d)-(f) Computed charge density at T_1-T_3 for ENC for U_{AC} = 8 kV.

Fig. 16 shows the computed corona inception criterion for the next cycle, which gives $U_i^p = 18.2$ kV and $U_i^n = 18.6$ kV. This deviates from the experimentally obtained corona inception voltage by 2.47% for the EPC and by 1.22% for the ENC. Due to the existence of space charge, the same electrode at different ratios of DC/AC voltages has the similar corona inception field but the different corona inception voltage.

Figs. 17(a)–17(c) show the space charge residual at T_5 for the EPC when U_{AC} = 16, 14, and 12 kV at D = 4 cm, and Figs. 17(d)–17(f) show the space charge residual at T_5 for the ENC. The maximum space charge density in the EPC at T_5 is always less than that in the ENC. As U_{AC} decreases, the space charge in the residues of both the EPC and ENC at T_5 increases because the maximum voltage of stage 2 decreases as the AC component decreases, thereby hindering the dissipation of space charge. Eventually, the space charge becomes more obstructed. This scenario explains the decrease in U_i for the positive and negative coronas as U_{AC} increases.

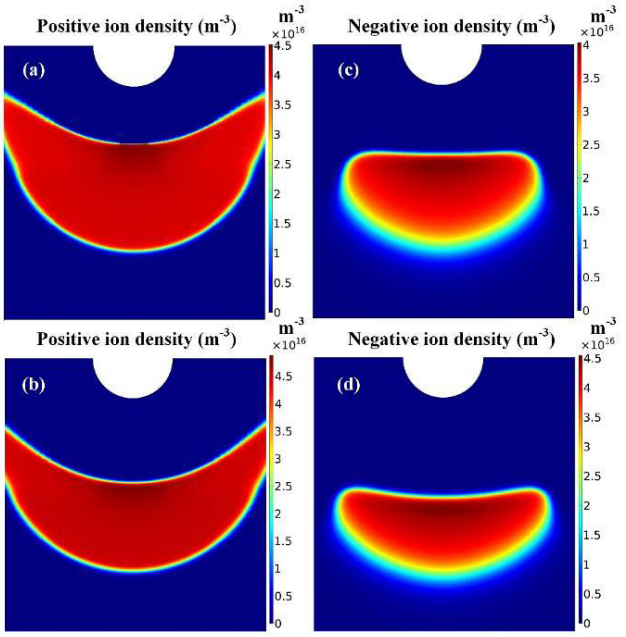

FIGURE 19. (a), (b) Computed charge density at T_4 for EPC for $U_{AC} = 8$ and 4 kV. (c), (d) Computed charge density at T_4 for ENC for $U_{AC} = 8$ and 4 kV.

D. THE CASE OF LOW U_{AC}

To investigate the variation in space charge when U_{AC} is small in Fig. 6(a) and Fig. 6(b), we consider the point T1-T4 in these figures. T_1 is the moment when the AC voltage is half the amplitude. T_2 is the point at the maximum AC voltage, T_3 is the point at the half cycle of AC voltage, At T_4, the potential difference between rod and plane is at its lowest point in the cycle.

The Fig. 18 shows the positive ion distribution of the EPC and the negative ion distribution of the ENC at T_1-T_3 moments when $U_{AC} = 8$kV. At T_1 moments, the voltage has not yet reached the corona inception voltage, the EPC and ENC gradually gather a portion of positive and negative ions near the rod head. At this time both the space charges are dominated by positive ions, so the negative ion order of magnitude in ENC is small. At T_2 moments, the corona begins to occur, and there is a sudden increase in the magnitude of both positive and negative ions in EPC and ENC. At this time, the space charge of both is still dominated by positive ions as shown in Fig. 12, Therefore, the magnitude of negative ions of ENC is small. After the T_2 moment, the negative ions of ENC gradually dominate the space charge. The positive ions of EPC and negative ions of ENC gradually drift outward under the action of electric field. During this process, the numbers of positive ions of EPC and negative ions of ENC decrease continuously. At T_3, the positive ions of EPC and negative ions of ENC are already with the same level.

At T_4, the potential difference between rod and plane is at its lowest point in the cycle. Fig. 19(a) and Fig. 19(b) show the distribution of the EPC space charge for $U_{AC} = 8$ and 4 kV, and Fig. 19(c) and Fig. 19(d) show the distribution of the ENC space charge for $U_{AC} = 8$ and 4 kV. As U_{AC} decreases, the space charge density of the EPC and ENC residues increases. The number of charges in residue of the EPC is 4.51×10^{16} m^{-3} for $U_{AC} = 8$ kV and 4.88×10^{16} m^{-3} for $U_{AC} = 4$ kV. The number of charges in the residue of the ENC is 4.04×10^{16} m^{-3} for $U_{AC} = 8$ kV and 4.55×10^{16} m^{-3} for $U_{AC} = 4$ kV. More charge remains in the EPC than in the ENC and obstructs the corona inception, which makes U_i^p higher than U_i^n.

IV. CONCLUSION

To summarize, the corona inception voltage and the variation in space charge near the rod under the combined DC-AC voltage differ from those under either DC or AC voltage. The results indicate that $U_i^n > U_i^p$ when U_{AC} is high, which is mainly due to there is more space charge residue for the equivalent negative corona than for the equivalent positive corona when U_{AC} is high. This space charge weakens the electric field near the rod electrode, which thereby hinders the equivalent negative corona inception. For high U_{DC}, there is more space charge for the equivalent positive corona than the equivalent negative corona, where the space charge displaces similarly to the DC corona, and $U_i^p > U_i^n$. It should be noted that the laws obtained in this paper are verified in short gap electrodes like rod-plane. However, whether the same law could be applied to long gap electrodes such as wire-plane needs to be further verified.

APPENDIX

TABLE 6. Simulation calculation parameters.

Parameters	value	
α (cm^{-1})	$3.9P\exp(-213/(\lvert E\rvert/P))$	$\lvert E\rvert/P<108$
	$14.5P\exp(-316/(\lvert E\rvert/P))$	$\lvert E\rvert/P\geq108$
η (cm^{-1})	$\max\{4.47/(\lvert E\rvert/P),\ 4.47\times10^{-3}(\lvert E\rvert/P)^2\}$	$\lvert E\rvert/P<10$
	$4.47\times10^{-3}(\lvert E\rvert/P)^2$	$10\leq\lvert E\rvert/P\leq50$
	$1.58\ (\lvert E\rvert/P)^{0.5}$	$50\leq\lvert E\rvert/P\leq90$
	$142/\ (\lvert E\rvert/P)^{0.5}$	$\lvert E\rvert/P>90$
β_{ep} (cm^3·s^{-1})	1×10^{-7}	
β_{np} (cm^3·s^{-1})	1×10^{-7}	
W_e (cm·s^{-1})	$-0.0382\lvert E\rvert-2.9\times10^5\lvert E\rvert/P$	
W_p (cm·s^{-1})	$1.43\times10^3\lvert E\rvert/P$	
W_n (cm·s^{-1})	$-3.3\times10^3\lvert E\rvert/P$	
D_e (cm^2·s^{-1})	1800	
D_p (cm^2·s^{-1})	0.046	
D_n (cm^2·s^{-1})	0.046	

where P is the atmospheric pressure in Torr.

REFERENCES

[1] T. Guillod, M. Pfeiffer, and C. M. Franck, "Improved coupled ion-flow field calculation method for AC/DC hybrid overhead power lines," *IEEE Trans. Power Del.*, vol. 29, no. 6, pp. 2493–2501, Dec. 2014.

[2] P. S. Maruvada and S. Drogi, "Field and ion interactions of hybrid AC/DC transmission lines," *IEEE Trans. Power Del.*, vol. PWRD-3, no. 3, pp. 1165–1172, Jul. 1988.
[3] X. Zhou, X. Cui, T. Lu, Y. Liu, X. Li, and C. Fang, "Measurement and modeling of low-frequency current from hybrid AC/DC corona," *IEEE Trans. Power Del.*, vol. 27, no. 3, pp. 1678–1686, Jul. 2012.
[4] M. A. Abouelatta, S. A. Ward, A. M. Sayed, K. Mahmoud, M. Lehtonen, and M. M. F. Darwish, "Fast corona discharge assessment using FDM integrated with full multigrid method in HVDC transmission lines considering wind impact," *IEEE Access*, vol. 8, pp. 225872–225883, 2020.
[5] C. Huang, H. Yin, P. Xu, B. Zhang, J. He, and J. Liu, "Prediction of radio interference from HVDC transmission lines based on corona discharge characteristics," *High Voltage*, vol. 5, no. 6, pp. 679–687, Dec. 2020.
[6] X. Bian, H. Li, X. Zhang, X. Cui, T. Lu, and W. Song, "Influence of fine particulate matter on the variation of surface morphologies of conductors subjected to positive DC voltages," *Appl. Phys. Lett.*, vol. 113, no. 20, Nov. 2018, Art. no. 204102.
[7] P. Xu, Y. Ma, J. Zhu, L. Zhao, B. Shen, and X. Bian, "Effect of TiO_2 coating on the surface condition and corona characteristics of positive DC conductors with particle matters," *High Voltage*, Jun. 2021, doi: 10.1049/hve2.12128.
[8] A. Kang, M. Tian, C. Li, J. Song, S. V. Suraci, W. Li, L. Lin, Z. Lei, and D. Fabiani, "Development and pattern identification of end-winding discharge under effect of relative humidity and temperature for HV motors," *High Voltage*, vol. 5, no. 4, pp. 434–443, Aug. 2020.
[9] K. He, X. Ma, J. Lu, W. Chen, L. Xie, Y. Ju, and L. Zhao, "Charging models for airborne suspended particles around HVDC lines," *High Voltage*, vol. 6, no. 2, pp. 348–357, Apr. 2021.
[10] S. Huang, Y. Liu, S. Chen, D. Liu, W. He, and B. Wan, "Corona onset voltage gradient of bundle conductors for EHV/UHV AC power lines in corona cages considering altitude correction," *CSEE J. Power Energy Syst.*, vol. 6, no. 3, pp. 693–703, Sep. 2020.
[11] Q. Hu, G. He, L. Shu, X. Jiang, Y. Liu, Y. Li, H. Peng, and W. Wu, "Minimum steady corona inception voltage calculation method under rain condition," *IET Gener., Transmiss. Distrib.*, vol. 12, no. 8, pp. 1783–1789, Apr. 2018.
[12] A. Eifert, T. Baier, and S. Hardt, "Small onset voltages in negative corona discharges using the edges of gold and aluminum foils as nano-structured electrodes," *Appl. Phys. Lett.*, vol. 103, no. 2, Jul. 2013, Art. no. 023114.
[13] C. Zhuang, Y. Zhang, and R. Zeng, "Electric field evaluation for slender conductors using collocation boundary element method," *CSEE J. Power Energy Syst.*, vol. 5, no. 4, pp. 483–488, Dec. 2019.
[14] B. Zhang, W. Li, J. He, and R. Zeng, "Study on the field effects under reduced-scale DC/AC hybrid transmission lines," *IET Gener. Transm. Distrib.*, vol. 7, no. 7, pp. 717–723, Jul. 2013.
[15] Y. Yang, J. Lu, and Y. Lei, "A calculation method for the hybrid electric field under UHVAC and UHVDC transmission lines in the same corridor," *IEEE Trans. Power Del.*, vol. 25, no. 2, pp. 1146–1153, Apr. 2010.
[16] W. Li, J. He, B. Zhang, R. Zeng, X. Li, and Q. Wang, "Calculation of the ion flow field of AC–DC hybrid transmission lines," *IET Gener., Transmiss. Distrib.*, vol. 3, no. 10, pp. 911–918, Oct. 2009.
[17] Y. Zheng, B. Zhang, and J. He, "Onset conditions for positive direct current corona discharges in air under the action of photoionization," *Phys. Plasmas*, vol. 18, no. 12, Dec. 2011, Art. no. 123503.
[18] D. B. Phillips, R. G. Olsen, and P. D. Pedrow, "Corona onset as a design optimization criterion for high voltage hardware," *IEEE Trans. Dielectr. Electr. Insul.*, vol. 7, no. 6, pp. 744–751, Dec. 2000.
[19] K. Yamazaki and R. G. Olsen, "Application of a corona onset criterion to calculation of corona onset voltage of stranded conductors," *IEEE Trans. Dielectr. Electr. Insul.*, vol. 11, no. 4, pp. 674–680, Aug. 2004.
[20] Z. He, J. Zhu, J. Zhu, X. Bian, and B. Shen, "Experiments and analysis of corona inception voltage under combined AC-DC voltages at various air pressure and humidity in rod to plane electrodes," *CSEE J. Power Energy Syst.*, vol. 7, no. 4, pp. 875–888, Jul. 2021, doi: 10.17775/CSEE-JPES.2020.03780.
[21] Z. Jie, H. Zichen, W. Jiale, and B. Xingming, "Experimental studies on effects of surface morphologies on corona characteristics of conductors subjected to positive DC voltages," *High Voltage*, vol. 5, no. 4, pp. 489–497, Aug. 2020.
[22] H. Liu, R. Liao, X. Zhao, L. Yang, and Y. Lin, "Corona onset criterion and surface electric field intensity characterized by space charge density," *IEEE Trans. Dielectr. Electr. Insul.*, vol. 26, no. 6, pp. 1973–1980, Dec. 2019.
[23] B. Dong, J. Song, C. Gao, Z. Zhang, Y. Gu, and N. Xiang, "Study on energized mixed-phase icing of CFCCW and its effect on AC corona onset voltage," *IEEE Access*, vol. 8, pp. 228349–228356, 2020.
[24] X. Bian, J. Zhu, W. Yang, S. Wan, L. Qi, X. Li, and H. Li, "The role of low air pressure in the variation of negative corona-generated space charge in a rod to plane electrode," *High Voltage*, vol. 3, no. 2, pp. 126–132, Jun. 2018.
[25] Y. Cui, C. Zhuang, and R. Zeng, "Electric field measurements under DC corona discharges in ambient air by electric field induced second harmonic generation," *Appl. Phys. Lett.*, vol. 115, no. 24, Dec. 2019, Art. no. 244101.
[26] X. M. Bian, S. W. Wan, L. Liu, Y. J. Wang, J. M. K. MacAlpine, L. Chen, L. M. Wang, and Z. C. Guan, "The role of charged particles in the positive corona-generated photon count in a rod to plane air gap," *Appl. Phys. Lett.*, vol. 103, no. 9, Aug. 2013, Art. no. 091504.
[27] F. J. Durán-Olivencia, F. Pontiga, and A. Castellanos, "Multi-species simulation of Trichel pulses in oxygen," *J. Phys. D, Appl. Phys.*, vol. 47, no. 41, Oct. 2014, Art. no. 415203.
[28] P. Dordizadeh, K. Adamiak, and G. S. P. Castle, "Numerical investigation of the formation of Trichel pulses in a needle-plane geometry," *J. Phys. D, Appl. Phys.*, vol. 48, no. 41, Oct. 2015, Art. no. 415203.
[29] W. L. Lama and C. F. Gallo, "Systematic study of the electrical characteristics of the 'Trichel' current pulses from negative needle-to-plane coronas," *J. Appl. Phys.*, vol. 45, no. 1, pp. 103–113, Jan. 1974.
[30] Z. Wang, T. Lu, X. Bian, H. Hiziroglu, and X. Li, "Modulation effect produced by adjacent AC voltage on the characteristics of negative corona current pulses in a wire-cylinder electrode configuration," *J. Electrostatics*, vol. 84, pp. 56–62, Dec. 2016.
[31] Z. Wang, T. Lu, X. Cui, X. Li, and H. Hiziroglu, "Influence of AC voltage on the positive DC corona current pulses in a wire-cylinder gap," *CSEE J. Power Energy Syst.*, vol. 2, no. 4, pp. 58–65, Dec. 2016.
[32] B. Qi, Z. Wei, C. Li, Y. Gao, and X. Zhang, "Influences of different ratios of AC-DC combined voltage on internal gas cavity discharge in oil-pressboard insulation," *IEEE Trans. Power Del.*, vol. 31, no. 3, pp. 1026–1033, Jun. 2016.
[33] H. Liu, Z. Xue, S. Li, Q. Li, D. He, T. Xia, and J. Guo, "Characteristics of partial discharge in oil-paper insulated needle plate electrode model under composite AC-DC voltage," *CSEE J. Power Energy Syst.*, vol. 6, no. 4, pp. 848–857, Dec. 2020.
[34] U. Straumann and C. M. Franck, "Ion-flow field calculations of AC/DC hybrid transmission lines," *IEEE Trans. Power Del.*, vol. 28, no. 1, pp. 294–302, Jan. 2013.
[35] X. Zhou, T. Lu, X. Cui, Y. Liu, and X. Li, "Simulation of ion-flow field at the crossing of HVDC and HVAC transmission lines," *IEEE Trans. Power Del.*, vol. 27, no. 4, pp. 2382–2389, Oct. 2012.
[36] Y. Tian, C. Liu, X. Huang, W. Tian, W. Cao, Y. Zhu, and L. Zhao, "The propagation of the ion-flow near the AC transmission lines," *IEEE Access*, vol. 8, pp. 146498–146509, 2020.
[37] F. Lv, J. Song, P. Wang, H. Ruan, and J. Geng, "Influencing factors of flow field of ionic wind induced by corona discharge in a multi-needle-to-net electrode structure under direct-current voltage," *IEEE Access*, vol. 7, pp. 123671–123678, 2019.
[38] Q. Gao, C. Niu, K. Adamiak, A. Yang, M. Rong, and X. Wang, "Numerical simulation of negative point-plane corona discharge mechanism in SF_6 gas," *Plasma Sour. Sci. Technol.*, vol. 27, no. 11, Nov. 2018, Art. no. 115001.
[39] T. Feng, W. He, and J. G. Wang, "FEM simulation of charge accumulation behaviours on polyimide surface in 10 kV negative high-voltage corona polarization process," *IEEE Access*, vol. 8, pp. 113151–113162, 2020.
[40] T. N. Tran, I. O. Golosnoy, P. L. Lewin, and G. E. Georghiou, "Numerical modelling of negative discharges in air with experimental validation," *J. Phys. D, Appl. Phys.*, vol. 44, no. 1, Jan. 2011, Art. no. 015203.
[41] P. Sattari, G. S. P. Castle, and K. Adamiak, "Numerical simulation of Trichel pulses in a negative corona discharge in air," *IEEE Trans. Ind. Appl.*, vol. 47, no. 4, pp. 1935–1943, Jul. 2011.
[42] H. Yin, B. Zhang, J. He, and C. Zhuang, "Modeling of Trichel pulses in the negative corona on a line-to-plane geometry," *IEEE Trans. Magn.*, vol. 50, no. 2, pp. 473–476, Feb. 2014.
[43] Y. Sha, Y. Zhou, L. Zhang, M. Huang, and F. Jin, "Measurement and simulation of partial discharge in oil-paper insulation under the combined AC–DC voltage," *J. Electrostatics*, vol. 71, no. 3, pp. 540–546, Jun. 2013.
[44] P. S. Maruvada, *Corona in Transmission Systems: Theory, Design and Performance*, 1st ed. Johannesburg, South Africa: Eskom Holdings, 2011, ch. 5, sec. 1, pp. 188–258.

[45] G. E. Georghiou, A. P. Papadakis, R. Morrow, and A. C. Metaxas, "Numerical modelling of atmospheric pressure gas discharges leading to plasma production," *J. Phys. D, Appl. Phys.*, vol. 38, no. 20, pp. 303–328, Oct. 2005.
[46] G. N. Aleksandrov, "Physical conditions for the formation of an alternating current corona discharge," *Sov. Phys., Tech. Phys.*, vol. 1, no. 8, pp. 1714–1726, 1956.

XUYUAN HE was born in Shanxi, China, in 1998. He received the B.S. degree in electrical engineering and automatization specialty from North China Electric Power University, Beijing, China, in 2019, where he is currently pursuing the M.S. degree in electrical engineering.

His research interests include electromagnetic environment of power transmission and transformation equipment.

YUNBO ZHOU was born in Liaoyang, Liaoning, China, in 1996. He received the B.S. degree in electrical engineering and automatization specialty from Northeast Agricultural University, Harbin, China, in 2018. He is currently pursuing the M.S. degree in electrical engineering with North China Electric Power University. His research interests include electromagnetic environment of power transmission and transformation equipment.

ZICHEN HE received the B.S. degree in electrical engineering and automatization specialty from North China Electric Power University, Beijing, China, in 2018, where he is currently pursuing the M.S. degree in electrical engineering.

His research interests include electromagnetic environment of power transmission and transformation equipment.

JIE ZHU received the B.S. degree in electrical engineering and automatization specialty and the M.S. degree in electrical engineering from North China Electric Power University, Beijing, China, in 2018 and 2021, respectively.

He is currently working with State Grid Yangzhou Power Supply Company, Yangzhou, Jiangsu, China. His research interests include electromagnetic environment of power transmission and transformation equipment.

LUXING ZHAO (Senior Member, IEEE) was born in Jilin, China, in 1983. He received the B.S. and M.S. degrees in electrical engineering from Wuhan University, Wuhan, China, in 2006 and 2008, respectively, and the Ph.D. degree from the School of Electrical and Electronic Engineering, North China Electric Power University, Beijing, China, in 2019. He is currently working with China Electric Power Research Institute, Beijing. He is an Excellent Technical Expert of China Electric Power Research Institute. His main research interest includes electromagnetic environment in power systems. He is also a Senior Member of China Society for Electrical Engineering.

BOYANG SHEN (Member, IEEE) received the dual Bachelor of Engineering (B.Eng.) degree (Hons.) in electrical and electronic engineering from Cardiff University, U.K., and North China Electric Power University (NCEPU), China, in 2012, the Master of Science (M.Sc.) degree in nuclear engineering from Imperial College London, U.K., in 2013, and the Master of Philosophy (M.Phil.) degree in electrical engineering and the Doctor of Philosophy (Ph.D.) degree in electrical engineering from the University of Cambridge, U.K., in 2014 and 2018, respectively.

He currently holds a Research Fellowship with Clare Hall. He is also a Research Associate with the Department of Engineering, University of Cambridge. He has published over 60 peer-reviewed journal articles. His research interests include electromagnetic field and its application in materials, the modeling of superconductors, electromagnetic characteristics and ac loss analysis of high-temperature superconductors (HTS), and the novel design of superconducting magnets and superconducting applications for electrical and energy systems.

Dr. Shen was awarded the IEEE Graduate Study Fellowship in Applied Superconductivity, which is the highest prize for graduates in the superconductivity community in the world, in 2018. In 2020, he was awarded the Royal Academy of Engineering (RAEng) Engineers Trust Young Engineer of the Year, which is one of the world highest honors for the scientists and engineers who have demonstrated excellence in the early stage of their career.

XINGMING BIAN (Member, IEEE) was born in Jiangsu, China, in 1985. He received the B.S. degree in electrical engineering from Huazhong University of Science and Technology, Wuhan, China, in 2006, and the Ph.D. degree from the Department of Electrical Engineering, Tsinghua University, Beijing, China, in 2012.

From 2012 to 2014, he was a Postdoctoral Researcher at the Graduate School at Shenzhen, Tsinghua University. He was a Visiting Scholar with the Department of Materials Science and Engineering, University of Illinois at Urbana–Champaign (UIUC), USA, in 2020. He is currently a Professor and a Ph.D. Supervisor with the School of Electrical and Electronic Engineering, North China Electric Power University. He has been presiding over several national scientific research projects during recent years. His research interests include electromagnetic field and its application in materials, electromagnetic compatibility, gas discharge physics, and new electric materials. He serves as a Board Member for journal IEEE Transactions on Dielectrics and Electrical Insulation, *High Voltage*, *CSEE Journal of Power and Energy Systems*, and IEEE Conference on Electrical Insulation and Dielectric Phenomena. He is a Winner of the Fok Ying-Tong Education Foundation and the Young Elite Scientists Sponsorship Program by China Association for Science and Technology.